Available online at www.sciencedirect.com
ScienceDirect
European Journal of Mechanics B/Fluids 26 (2007) 64–82

# Numerical studies of the instability and breakdown of a boundary-layer low-speed streak

Luca Brandt

*KTH Mechanics, S-10044 Stockholm, Sweden*

Received 29 August 2005; accepted 19 April 2006

Available online 6 September 2006

**Abstract**

The experimental configuration in [M. Asai, M. Minagawa, M. Nishioka, The instability and breakdown of a near-wall low-speed streak, J. Fluid Mech. 455 (2002) 289–314] is numerically reproduced in order to examine the instability of a single low-speed streak in a laminar boundary layer and to investigate the resulting generation of coherent structures. Such a configuration is chosen since the experimental data show that the two instability modes, varicose and sinuous, are of comparable strength. The instability characteristics are retrieved from the simulation of the flow impulse response. The varicose instability is associated to higher frequencies and lower group velocities than those of the sinuous modes. The latter are less affected by the diffusion of the streak mean shear and are amplified for a longer streamwise distance. Analysis of the perturbation kinetic energy production reveals that both the varicose and the sinuous instability are driven by the work of the Reynolds stress against the wall-normal shear of the streak. The base flow considered here therefore presents an exception to the common knowledge, supported by several previous studies, that the sinuous instability is associated to the streak spanwise shear. The vortical structures at the late stage of the varicose breakdown are identified from the numerical data. By comparing them with those pertaining to other transition scenarios, it is confirmed that streaks and streamwise vortices are universal features of boundary layer transition.


*Keywords:* Boundary layers; Transition to turbulence; Stability; Streamwise streaks; Hairpin vortices

## 1. Introduction

The occurrence and instability of low-speed streaks are now identified as a key element in transition to turbulence and in the dynamics of turbulence in wall-bounded shear flows. Indeed low-speed streaks are observed at the late stages of different transition scenarios and streak breakdown is one of the phases of the regeneration cycle which is believed to sustain a turbulent flow. The so-called low-speed streaks are perturbations elongated in the streamwise direction consisting of negative streamwise velocity perturbation which induce a localised region of decelerated flow. These areas are always surrounded by regions of large shear both in the wall-normal and in the spanwise direction. The corresponding inflectional velocity distributions are thus able to support inviscid instabilities.

Streaks were first visualised in turbulent boundary layers by Kline et al. [29]. Kim et al. [28] later showed the importance of local intermittent inflectional instability in the bursting events which are associated with periods of strong

*E-mail address:* luca@mech.kth.se (L. Brandt).

0997-7546/$ – see front matter 
doi:10.1016/j.euromechflu.2006.04.008

turbulent production. These authors observed different oscillatory types of motion of the streaks. Swearingen and Blackwelder [43] compared and related the modes observed in [28] to the secondary varicose and sinuous instability of streamwise vortices measured during transition on a concave wall. These two types of instability modes appear in a spanwise symmetric (varicose) or antisymmetric (sinuous) pattern with respect to the underlying streak. The varicose instability is usually related to wall-normal inflectional profiles, whereas the sinuous to spanwise inflectional profiles, the exception being provided by the present work. Recent studies on the instability of a base flow generated by the superposition of a turbulent mean flow and the streaky structures [44,40,27] have found that the dominating instability is sinuous. Moreover, the flow structures observed in the numerical simulations by Jiménez and Pinelli [24] and Jiménez and Simens [25] in limiting conditions for the turbulence to be self-sustained are also similar to those observed when the sinuous streak instability is studied. On the other hand, hairpin vortices, associated to a symmetric distribution of the perturbations growing on the streak are also found in turbulent flows (e.g. [37,13,42]).

The appearance of low-speed streaks and hairpin vortices are also observed at the final stages of transition initiated by the growth of Tollmien–Schlichting waves. In this scenario, transition to turbulence takes place as a high-frequency secondary instability with the breakdown of thin internal shear layers into hairpin vortices (first identified in the experiment Nishioka et al. [34].) The numerical simulations by Sandham and Kleiser [38] and Rist and Fasel [36] reproduced the experiments and also found hairpin (or $\Lambda$-) vortices as fundamental structures triggering the occurrence of near-wall turbulence.

Streak instability is also found as the secondary instability process occurring in bypass transition in boundary layers. Transition is defined as bypass when it is not initiated by the exponential growth of the unstable Tollmien–Schlichting waves. This scenario is more likely to occur in the presence of high levels of free-stream perturbation and it is characterised by the appearance of elongated streamwise streaks inside the boundary layer (see among others [33]). It is now understood that the growth of streaks can be explained successfully by the theory of non-modal growth (see [39]) and it is due to the so-called lift-up effect [30]. The instability of steady and spanwise periodic streaks due to non-modal growth of optimally growing streamwise vortices has been investigated by Andersson et al. [1]. These authors identified the sinuous instability as the most dangerous. Brandt and Henningson [10] performed numerical simulations to investigate the late stages of the breakdown triggered by the sinuous streak instability and identified the relevant flow structures. Not surprisingly, they are very similar to those observed for turbulent flows. The recent numerical simulations of transition in a boundary layer subject to free-stream turbulence in [11] enabled to identify the structures at the streak breakdown, something difficult to do in an experiment due to the random nature of their appearance. Both sinuous and varicose modes are observed, with the former being more likely to occur. In summary, one can note that thus far the analysis performed on transition and turbulent streaks have revealed the presence of both symmetries at the breakdown, while linear stability analysis have mainly considered flows where one of the two modes is dominating, e.g. [44,1] for sinuous modes and [42] for their varicose counterpart.

To shed some light on the dynamics of near-wall turbulence and on the mechanism by which coherent structures are generated and sustained, Asai et al. [2] conducted an experimental study on the instability of a single low-speed streak in a laminar boundary layer. Such a streak is created by using a small piece of screen set normal to the wall. It should be emphasised here that this is not a configuration in which transient growth is expected since there is little steady streamwise vorticity. These authors observed both instability modes and compared the two. They found that when the streak width is narrow the flow becomes more unstable to sinuous perturbations than to varicose and that the amplification of the sinuous modes is sustained for a longer downstream distance. Visualisations also demonstrate that the varicose mode leads to the formation of hairpin vortices with a pair of counter-rotating streamwise vortices. The antisymmetric mode evolves into quasi-streamwise vortices with vorticity of alternating sign, in agreement with the findings from the simulations by Jiménez and Simens [25]; Brandt and Henningson [10]; Schoppa and Hussain [41].

In the present paper, the experimental configuration in [2] is numerically reproduced with a twofold objective.

(i) Analyse the instability features and underlying mechanism for a flow where both instabilities are present and of comparable strength.
(ii) Extract from the numerical results more detailed data about the characteristic flow structures at the late stages of the breakdown initiated by the varicose instability.

These are compared to those pertaining to other transition scenarios, completing the available picture on the vortical structures at breakdown.

The paper is organised as follows. In Section 2 the numerical method and the disturbance generation procedure are introduced. Three types of simulations are performed. The low-speed streak is first generated by simulating the screen at the wall in the experiment by Asai et al. [2]. The instability features are retrieved from the numerical simulation of the flow impulse response where the streak profiles extracted at different streamwise positions are assumed as parallel base flow. The breakdown is triggered by implementing time periodic blowing and suction at the wall. The characteristics of the streaky base flows are presented in Section 3, while the instability features are presented in Section 4. Here, the instability mechanism is analysed by looking at the equation governing the evolution of the perturbation kinetic energy. The streak breakdown is discussed in Section 5. The paper ends with a summary of the main conclusions.

## 2. Numerical method and diagnostic tools

### 2.1. Numerical scheme

The simulation code employed for the present computations uses spectral methods to solve the three-dimensional, time dependent, incompressible Navier–Stokes equations and it is presented in [31]. The code has now been used for more than a decade for the direct numerical simulation of both transitional and turbulent flows. Detailed descriptions of the algorithm adopted for spatially evolving boundary layers can also be found in [4,10].

To correctly account for the downstream boundary layer growth a spatial technique is necessary. This requirement is combined with the periodic boundary condition in the streamwise direction by the implementation of a "fringe region", similar to that described by Bertolotti et al. [6]. In this region, the flow is smoothly forced to the prescribed inflow velocity vector. This is normally a boundary layer profile, but can also contain a disturbance. For further details on this technique see [31,35]. In order to set the free-stream boundary condition at some $y = y_{\max}$ closer to the wall, a generalisation of the boundary condition used by Malik et al. [32] is implemented.

To simulate the streak impulse response, the code has been changed in order to solve the Navier–Stokes equations linearised around a parallel basic flow of streaky nature $(U, V, W) = (U(y, z), 0, 0)$, i.e. a basic flow consisting only of the streamwise velocity component, whose shape varies in both the wall-normal and spanwise direction. Owing to the assumption of parallel flow, the spatial technique introduced above is not necessary for the instability computations. Further, for this type of simulations homogeneous Dirichlet or Neumann boundary conditions are used at the free-stream boundary.

### 2.2. Disturbance generation

The presented numerical implementation provides several possibilities for disturbance generation. For the simulation presented here three different types of excitation have been used. A steady forcing, modelling the screen in the experiment by Asai et al. [2], is employed to generate the low-speed streak. Its instability is studied by simulating the impulse response where the perturbations are introduced as initial condition. To trigger the streak breakdown, time-periodic blowing and suction at the wall is implemented through non-homogeneous boundary conditions.

To induce a momentum loss in the near-wall region of the Blasius laminar boundary layer, a localised volume forcing is added to the streamwise component of the momentum equation. This forces the streamwise velocity component $u$ to be very low while growing linearly in the wall-normal direction $y$. Here, the coordinates are made non-dimensional with the boundary-layer displacement thickness $\delta_0^*$ at the inflow of the computational domain whereas the velocities are divided by the free-stream speed $U_\infty$. The forcing takes the following form

$$F(x, y, z) = A_x S\left(\frac{y_{\text{loc}} + y_{\text{scale}} - y}{y_{\text{scale}}}\right)\left(\frac{y}{y_{\text{loc}}} - \frac{u}{u_f}\right)u_f S\left(\frac{t}{t_{\text{scale}}}\right)g(x, y), \tag{1}$$

where $g$ determines the behaviour in the streamwise, $x$, and spanwise, $z$, directions and $S$ is used in several instances to smoothly introduce the forcing. They are defined as

$$g(x, z) = \exp\left[-\left((x - x_{\text{loc}})/x_{\text{scale}}\right)^2\right]\left[S\left(\frac{z + z_{\text{loc}} + z_{\text{scale}}/2}{z_{\text{scale}}}\right) - S\left(\frac{z - z_{\text{loc}} + z_{\text{scale}}/2}{z_{\text{scale}}}\right)\right], \tag{2}$$

$$S(a) = \begin{cases} 0 & a \leqslant 0, \\ 1/[1 + \exp(\frac{1}{a-1} + \frac{1}{a})] & 0 < a < 1, \\ 1 & a \geqslant 1. \end{cases} \tag{3}$$

In the expressions above, $u_f$ is the value of $u$ attained at the distance $y_{\text{loc}}$ from the wall, where the forcing starts to decay to zero in $y_{\text{scale}}$. The forcing is localised around $x_{\text{loc}}$ and is active in the spanwise region between $-z_{\text{loc}}$ and $+z_{\text{loc}}$. The parameter $z_{\text{scale}}$ is introduced in order to smoothly attenuate the forcing amplitude and thus limit the numerical resolution required. The time-dependent function $S(\frac{t}{t_{\text{scale}}})$ has been used to ensure a smooth turn on of the forcing.

The following set of values is used for the parameters introduced above. $y_{\text{loc}} = 1$, $y_{\text{scale}} = 0.4$, $x_{\text{loc}} = 57.19$, $x_{\text{scale}} = 1.4$, $z_{\text{loc}} = 1.82$ and 1.21, $z_{\text{scale}} = 0.35$, $A_x = 0.8$, $u_f = 0.07$, $t_{\text{scale}} = 300$. They have been chosen in order to match the experimental configuration in [2]. Note that the computational inlet is at $Re_{\delta_0^*} = 549.35$ and therefore $\delta_0^* = 2.1$ mm if one chooses the value of the free-stream velocity and viscosity corresponding to those in the experiments. In particular, the two values of $z_{\text{loc}}$ used represent the 7.5 mm- and 5 mm-wide screens used in [2].

The initial condition used to compute the streak linear impulse response is identical to that used in [8]. To mimic forcing by a delta-function in time and space, this is defined in terms of a stream function as

$$\psi(x, y, z; 0) = A_i \bar{x} \bar{y}^3 \bar{z} \exp\bigl(-\bar{x}^2 - \bar{y}^2 - \bar{z}^2\bigr), \tag{4}$$

where $\bar{x} = (x - x_0)/l_x$, $\bar{y} = y/l_y$ and $\bar{z} = (z - z_0)/l_z$. The corresponding velocity components are given by $(u, v, w) = (0, \psi_z, -\psi_y)$ and the amplitude $A_i$ is set to 1 since the linearised Navier–Stokes equations are integrated. The length scales, typically $l_x = 5$, $l_y = 2$ and $l_z = 1.5$ have been chosen small enough to reproduce a localised impulse within the limits of a good resolution in the truncated spectral space of the numerical simulations. Note also that since the eigenfunctions depend on both $y$ and $z$, a strong localisation is not needed in these directions. Moreover, the disturbance is centred around $z = z_0$, which is chosen to lie off axis in one of the two regions of strongest streak spanwise shear so that no particular symmetry is enforced on the solution. The initial condition (4) consists of two counter-rotating streamwise vortex pairs. It has been used previously by Henningson et al. [17]; Bech et al. [3] and almost in the same form by Breuer and Haritonidis [12].

To force the streak instability modes and be able to follow their breakdown, nonhomogeneous boundary conditions for the wall-normal velocity component are implemented. In particular, to force perturbations symmetric with respect to the middle of the low-speed streak ($z = 0$) the following expression is used

$$v_{\text{var}}(x, 0, z) = v_{\text{wall}} \exp\bigl[-\bigl((x - x_{\text{sb}})/x_{\text{sc}}\bigr)^2\bigr] \exp\bigl[-(z/z_{\text{sc}})^2\bigr] \sin(\omega t), \tag{5}$$

whereas the function $v_{\text{sin}} = v_{\text{var}}(x, 0, z) \cdot z$ is used to force the antisymmetric sinuous instability. The blowing/suction is localised around $x_{\text{sb}}$ at frequency $\omega$. The parameter $v_{\text{wall}}$ determines its strength, while $x_{\text{sc}}$ and $z_{\text{sc}}$ its spatial extent. The following values are used to trigger the varicose breakdown $\omega = 0.36$, $v_{\text{wall}} = 0.035$, $x_{\text{sb}} = 68$, $x_{\text{sc}} = 2.5$ and $z_{\text{sc}} = 0.5$, while the values $\omega = 0.19$, $v_{\text{wall}} = 1.2$, $x_{\text{sb}} = 68$, $x_{\text{sc}} = 4.5$ and $z_{\text{sc}} = 1$ are chosen in the case of the sinuous breakdown.

### 2.3. Numerical resolution and computational domain

The box sizes and resolutions used for the simulations presented in this paper are displayed in Table 1. The inlet of the computational box which is set to $Re_{\delta_0^*} = 549.35$ for all cases under consideration. In all simulations performed, the length of the fringe region is chosen to be 50.

Box1 is used for the simulations of the basic flow with the steady forcing in (1). Box2 and Box3 are used to compute the streak breakdown. For this type of simulations the resolution is increased also by decreasing the streamwise extension of the computational domain. The computation of the linear impulse response are typically performed with Box4, and higher resolution was used to check the results in the case of the most unstable streak profiles.

### 2.4. Analysis of the linear impulse response

To retrieve the linear temporal and spatio-temporal instability features directly from the numerical simulation of the flow impulse response, the technique developed by Delbende et al. [16] and Delbende and Chomaz [15] is applied.

Table 1
Resolution and box dimensions for the simulations presented

| | $xl \times yl \times zl$ $\delta_0^*$ | $nx \times ny \times nz$ (resolution) | $Re_{\delta_0^*}$ |
|---|---|---|---|
| Box1 | $350 \times 9 \times 15$ | $648\times 73 \times 128$ | 549.35 |
| Box2 | $250 \times 9 \times 15$ | $648\times 73 \times 128$ | 549.35 |
| Box3 | $250 \times 9 \times 15$ | $800\times 91 \times 128$ | 549.35 |
| Box4 | $600 \times 9 \times 15$ | $512\times 73 \times 96$ | 549.35 |

The box dimensions include the fringe region and are made dimensionless with respect to $\delta_0^*$, the displacement thickness at the beginning of the computational box. The length of the fringe region is 50 for all cases under consideration. The total number of Fourier modes is indicated, corresponding to $nx/2$ or $nz/2$ conjugate pairs.

This was extended to the case of a three-dimensional unidirectional base flow in [8]. The analysis is performed in physical space according to the original definitions of perturbation evolution in the laboratory frame (see [21]), without resorting to the spectral theory of absolute and convective instability.

Within a temporal framework the wavenumber $k_x$ is given real and the frequency $\omega(k_x)$ is complex and unknown. Let us define the amplitude spectrum of the perturbations

$$\tilde{e}(k_x, t) = \left( \int_0^{y_{\max}} \int_0^{\lambda_z} \left| \tilde{q}(k_x, y, z, t) \right|^2 \mathrm{d}y \, \mathrm{d}z \right)^{1/2}, \tag{6}$$

where $q(x, y, z, t)$ may be any flow perturbation variable, e.g. a single velocity component or the square root of the total kinetic energy, and $\tilde{q}(k_x, y, z, t)$ its Fourier transform in the streamwise direction. For large times the asymptotic exponential behaviour is attained and, if a well separated temporal branch is present, the temporal growth rate $\omega_i$ of each $k_x$-component is given by

$$\omega_i(k_x) \sim \frac{\partial}{\partial t} \ln \tilde{e}(k_x, t), \quad t \to \infty, \tag{7}$$

where $\omega_i$ is the imaginary part of $\omega$. To compute the real part $\omega_r(k_x)$, corresponding to the angular frequency of the temporal mode, we consider the phase distribution

$$\phi(k_x, t) = \arg \tilde{q}(k_x, y_0, z_0, t), \quad 0 \leqslant \phi(k_x, t) \leqslant 2\pi, \tag{8}$$

where $y_0$ and $z_0$ define with the position of maximum perturbation at the wavenumber $k_x$ of maximum perturbation energy. The frequency is calculated according to

$$\omega_r(k_x) \sim \frac{\partial}{\partial t} \phi(k_x, t), \quad t \to \infty. \tag{9}$$

In the *spatio-temporal* formulation the development of the wave packet along rays of specific given velocity $x/t = v$ is considered. This is equivalent to the investigation of modes of real group velocity $v$, as reviewed, for instance, in [22,21]. In order to demodulate the wave packet and define its amplitude unambiguously, it is convenient to introduce the analytical complex field variable $\bar{q}(x, y, z, t)$ associated with $q(x, y, z, t)$ through the convolution

$$\bar{q}(x, y, z, t) = \left[ \delta(x) + \frac{i}{\pi x} \right] * q(x, y, z, t), \tag{10}$$

where the symbol $*$ designates the convolution operator with respect to $x$. The complex field $\bar{q}(x, y, z, t)$ generalises the complex exponential representation of a sine wave to an arbitrary real function $q(x, y, z, t)$. As in the temporal analysis, the integration of the analytical field $\bar{q}$ in the cross-stream $(y, z)$ plane then yields the amplitude $Q$ defined by

$$Q(x, t) = \left( \int_0^{y_{\max}} \int_0^{\lambda_z} \left| \bar{q}(x, y, z, t) \right|^2 \mathrm{d}y \, \mathrm{d}z \right)^{1/2}. \tag{11}$$

According to steepest-descent arguments [5], the long-time behaviour of the wave packet along each spatio-temporal ray $x/t = v$ is

$$Q(x,t) \propto t^{-1/2} e^{i[k_x(v)x - \omega(v)t]}, \quad t \to \infty, \tag{12}$$

where $k_x(v)$ and $\omega(v)$ represent the complex wavenumber and frequency travelling at the real group velocity $v = x/t$. In (12), the real part of the exponential

$$\sigma(v) = \omega_i(v) - k_{x,i}(v)v \tag{13}$$

denotes the temporal growth rate observed while travelling at the group velocity $v$ and it can be evaluated for large $t$ directly from the amplitude $Q$ in (12) as

$$\sigma(v) \sim \frac{\partial}{\partial t} \ln\bigl[t^{1/2} Q(vt,t)\bigr]. \tag{14}$$

In unstable flows, $\sigma > 0$ for some range of $v$. The curves $\sigma(v)$ contain all the information characterising the spatio-temporal growth of the wave packet. Its extent, in fact, is delineated by the rays along which neutral waves are observed. These velocities are denoted $v^-$, the trailing edge velocity of the wave packet, and $v^+$, the leading edge velocity of the wave packet.

## 3. Base flows

The steady flow induced by the forcing in expression (1) is presented in Fig. 1. Throughout the paper the different physical quantities are made non-dimensional with respect to the free-stream velocity and the boundary layer displacement thickness $\delta_0^*$ at the inflow of the computational domain. As mentioned above, this corresponds to 2.1 mm if one wishes to compare the present results with the experiment by Asai et al. [2]. The flow in Fig. 1 is induced by the wider forcing ($z_{\mathrm{loc}} = 1.82$ in Eq. (2)), mimicking the 7.5 mm-wide screen used in the experiment. The selected locations correspond to streamwise stations located 30, 50 and 100 mm downstream of the screen. At these locations the details

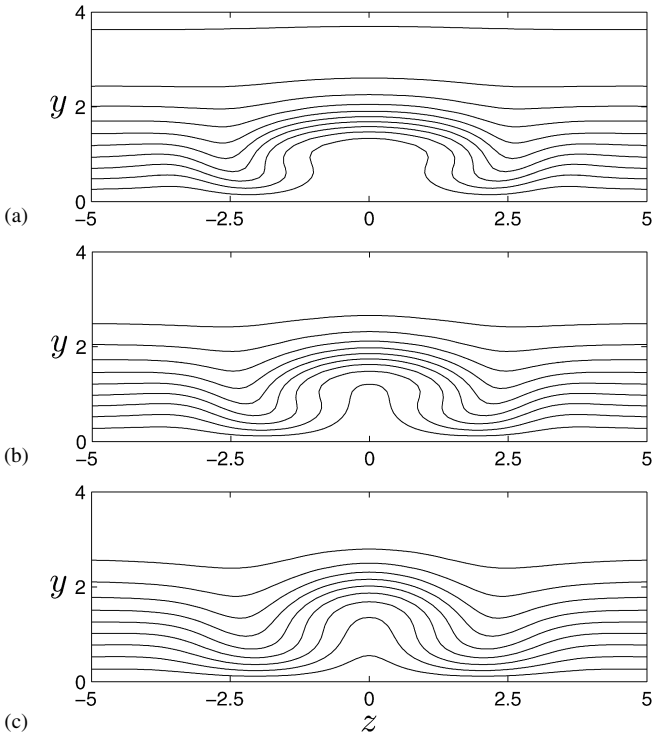


Fig. 1. Contour levels of the streamwise velocity component for the streak induced by the wider screen ($\Delta z = 3.6$) at (a) $x = 71.5$, (b) $x = 81$ and (c) $x = 104.8$. Minimum contour level is 0.1 and the contour spacing is 0.1.

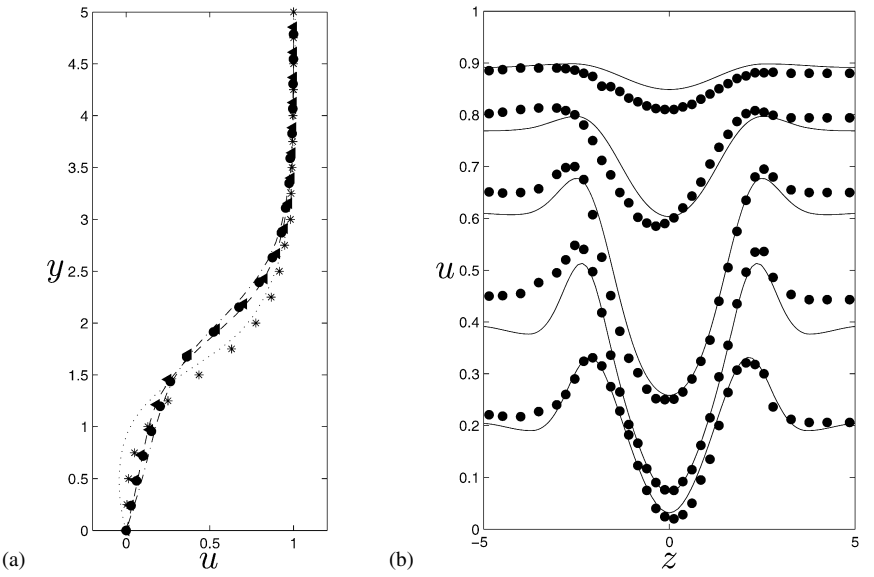


Fig. 2. Comparison with the experimental results in [2]. (a) Wall-normal velocity profiles at $z = 0$. $x = 67$: $*$, experimental data; $\cdots\cdots$, numerical results. $x = 95.3$: $\blacktriangleleft$, experimental data; $---$, numerical results. $x = 114.3$: $\bullet$, experimental data; $-\cdot-$, numerical results. (Cf. Fig. 4 in [2].) (b) Spanwise distribution of the streamwise velocity at $x = 81$ for $y = 2.5, 2, 1.5, 1, 0.5$. ($\bullet$, experimental data). (Cf. Fig. 2(b) in [2].)

of the disturbance generation have become negligible and a region of lower streamwise velocity is clearly observed. This will be the object of the stability analysis performed. Comparison with the experimental data by Asai et al. [2] is displayed in Fig. 2, where both wall-normal and spanwise streamwise velocity profiles are reported. Note that just behind the artificial numerical obstacle a small region of negative streamwise velocity can be observed. It can also be seen that the low-speed streak is followed on its sides by a acceleration of the flow, as observed also by Asai et al. [2]. The flow is basically unaffected further away in the span, so that, despite the use of periodic boundary conditions, the low-speed streak considered here can be seen as isolated. The effect of the streak periodicity and confinement has been investigated recently by Brandt et al. [9]. The results indicate that the streak instability characteristics are unaffected by changes in the spanwise extension of the domain if this is chosen to be sufficiently wide.

The downstream evolution of the wall-normal and spanwise shear associated to the streak is shown in Fig. 3. As shown below, the instability features are closely related to the shear of the basic flow. The wall-normal shear, $\frac{\partial U}{\partial y}$, is displayed in a plane perpendicular to the wall, along the symmetry line at $z = 0$ and at the streamwise stations for which the streak instability will be analysed (see Section 4). The shear attains its maximum value above the screen and decays downstream, while slowly diffusing away from the wall. The spanwise shear, $\frac{\partial U}{\partial z}$, is displayed in a plane parallel to the wall at $y = 1$ in Fig. 3(b). It also reaches its maximum at the location of the artificial obstacle. Positive shear, increasing streamwise velocity, is located on the positive flank of the low-speed streak whereas negative shear can be found for negative values of the $z$-coordinate. Further away from the symmetry line, weaker negative and positive shear are located on the positive and negative sides, respectively. They are associated to the flow acceleration mentioned above. It is interesting to note that the wall-normal shear is stronger than its spanwise counterpart but decays faster. The spanwise shear seems to set to an almost constant value for $x > 90$. Similar considerations apply for the case of the streak induced by the narrow screen. The spanwise shear is about 30% higher in this case, whereas the wall-normal shear attains similar values on the symmetry line and its decay is only slightly faster if compared to the case of the streak induced by the wider screen.

## 4. Streak instability

### *4.1. Temporal instability*

The flow impulse response is computed for the streak profiles $U(y, z)$ extracted at five streamwise locations $x = 71.5$, $x = 81$, $x = 95.3$, $x = 104.8$ and $x = 114.3$. These correspond to a distance of 30, 50, 80, 100 and 120 mm

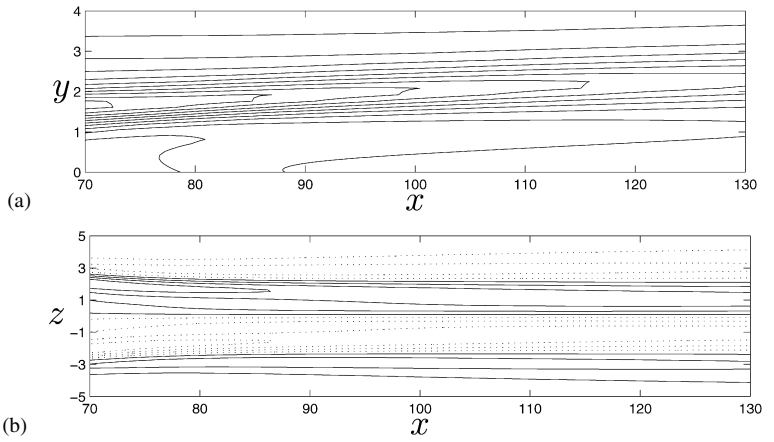


Fig. 3. (a) Wall-normal shear $\frac{\partial U}{\partial y}$ for the streak induced by the wider screen in a plane perpendicular to the wall at $z = 0$ (symmetry line). The minimum contour level is 0.05, the maximum is 0.95 and the contour spacing is 0.1. (b) Spanwise shear $\frac{\partial U}{\partial z}$ for the streak induced by the wider screen in a plane parallel to the wall at $y = 1$. The minimum contour level is $-0.35$, the maximum is 0.35 and the contour spacing is 0.1. Dotted lines indicate negative values.

downstream of the screen (located at $x = 57$), if one wishes to compare with the experiments in [2]. In this section, the results of the temporal stability analysis are presented.

The temporal growth rates $\omega_i$ and phase speeds $c_r$ versus the streamwise wavenumber $k_x$ of the varicose modes for the two streaky basic flows under consideration are shown in Fig. 4, whereas the instability characteristics of the sinuous modes are displayed in Fig. 5. To facilitate the comparisons the same values on the axis are used in each plot. The growth rates of the varicose instability decrease significantly downstream: at $x = 114.3$ the streak induced by the wider screen is stable, whereas the streak induced by the narrow screen is already stable at $x = 95.3$ (Fig. 4(a) and (c)). The maximum growth rates are attained just downstream of the screen for streamwise wavenumbers $k_x$ of about 0.8. Typical phase speeds range between 0.4 and 0.6, with values increasing with $x$. In Fig. 4(a) and (c), a second branch of weaker instability can be seen at low streamwise wavenumbers. By examining the corresponding phase speeds, it can be suggested that these waves might be modified Tollmien–Schlichting waves in the case of the narrow streak at the locations furthest downstream (see Fig. 4(d)). Conversely, the strong varicose instability, see the most upstream locations in Fig. 4(b), is followed by modes of larger phase speed at low values of $k_x$. Note that, owing to the low growth rates, it is difficult to obtain converged results from the streak impulse response when perturbations of larger wavenumber or of different symmetry have larger amplification rates (see dash–dotted line in Fig. 4(c)).

The growth rates of the sinuous modes are more persistent in the streamwise direction, as also observed in the experiment by Asai et al. [2]. A decrease of the amplification while moving downstream is evident only for the narrow streak, Fig. 5(c). When comparing with the varicose modes, the most unstable wavenumbers are smaller and the phase speeds slightly larger. From the results above one can conclude that the most unstable mode is of varicose symmetry for $x < 95$ in the case of the wide streak, whereas the sinuous instability becomes dominant already at $x > 81$ for the narrow streak.

The circular frequency $w_r = k_x c_r$ of the most amplified varicose waves is about 120 Hz and is almost independent of $x$ for the wider streak, whereas it is about 135 Hz for the narrow streak. These values are only slightly larger than those obtained with spatial stability analysis by Asai et al. [2]. The frequency of the most amplified sinuous modes varies between 40 and 60 Hz for the wider streak and between 50 and 65 Hz for the narrow streak. These values and the fact that the sinuous mode has larger frequency for the narrow streak are again in good agreement with the results in [2]. Moreover, at $x = 81$ the varicose instability on the wider streak is characterised by a maximum growth rate about twice as large than that pertaining to the sinuous modes. The latter, at this upstream station, have almost the same growth rate for the two streak under consideration, as in the experimental results. One can therefore conclude that the numerical streaks computed here reproduce the main features of the streaks in the experiment.

The cross-stream distribution of the streamwise velocity fluctuations for the varicose temporal mode of streamwise wavenumber $k_x = 0.84$ and for the sinuous mode of streamwise wavenumber $k_x = 0.33$ are displayed in Fig. 6(a) and (b), respectively. Contour levels of the underlying streak profile, extracted at $x = 81$, are also shown for comparison.

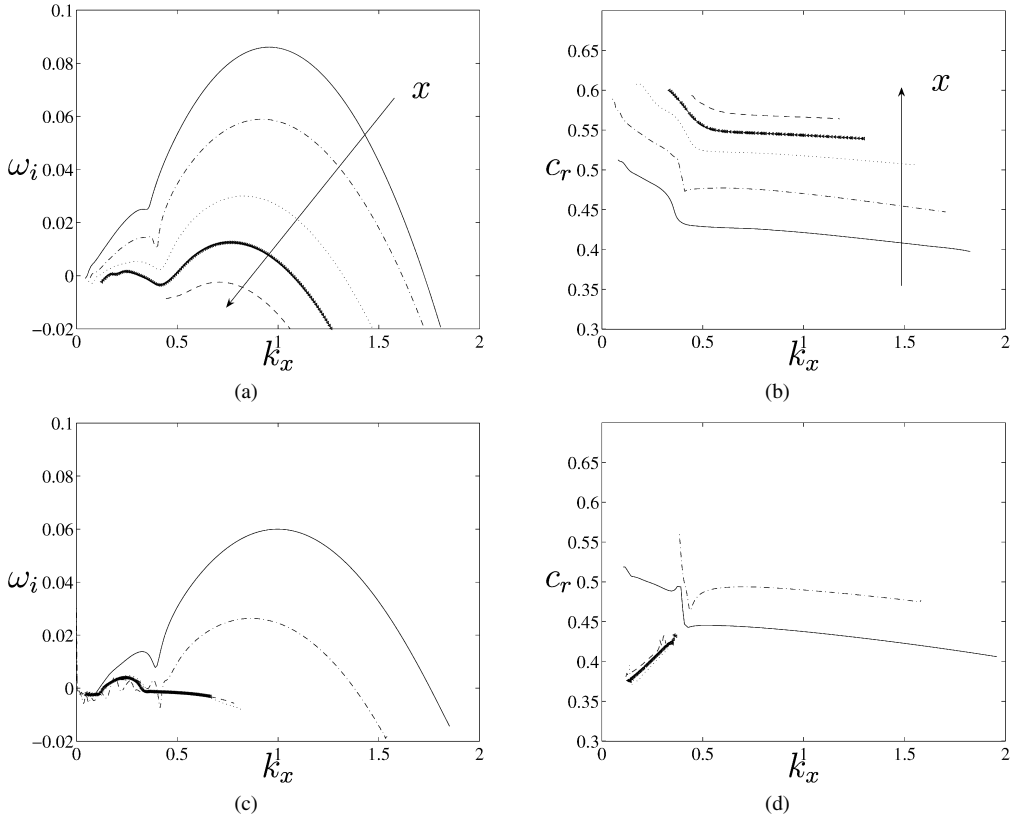


Fig. 4. Temporal growth rates $\omega_i$ and phase speeds $c_r$ versus the streamwise wavenumber $k_x$ for the varicose instability modes pertaining to the streak induced by the wider screen (a) and (b), and by the narrow screen (c) and (d). The streak profiles are extracted at $x = 71.5$ (solid line), $x = 81$ (dash–dotted line), $x = 95.3$ (dotted line), $x = 104.8$ (line with symbols) and $x = 114.3$ (dash line).

The velocity fluctuations pertaining to the symmetric instability mode are largest in the horizontal layer where the wall-normal shear attains its maximum values ($y \approx 1.5$) and also relevant in the region on the flanks of the low-speed streak where the spanwise shear is maximum. The antisymmetric perturbation is also largest in correspondence with the horizontal layer of maximum wall-normal shear with peaks on the two sides. Surprisingly, for this type of streak the largest sinuous fluctuations are not located on the region of maximum spanwise shear as observed in the case of optimal streak in [1,8]. An explanation for this observation is given below.

### *4.2. Spatio-temporal instability*

To determine the spatio-temporal instability properties of the streaks, the wave packet induced by the localised disturbance (4) is analysed in physical space along rays of group velocity $x/t = v$, as outlined in Section 2.4. The computed temporal growth rates are displayed in Figs. 7 and 8 for the varicose and sinuous instability, respectively.

The trailing edge velocity $v^-$ of the wave packet is in all cases positive and therefore it may immediately be concluded that the instability is of convective nature. The growth rate curves are close to parabola. In the case of the largest varicose instabilities, the trailing edge velocity is about 20% of the free-stream velocity, whereas the leading edge velocity $v^+$ is about $0.6U_\infty$. The spreading rate velocity of the wave packet $\Delta v = v^+ - v^-$ decreases for increasing $x$, i.e. with decreasing amplifications. The maximum growth rates occur at a group velocity varying between 0.4 and 0.5 of the free-stream velocity. The sinuous instability wave packet is characterised by slightly larger propagation velocities and by a somewhat larger scatter among the different streak profiles under considerations. The wave-packet trailing-edge velocity varies between 20% and 45% of $U_\infty$ for the least unstable basic flows at $x = 114.3$, whereas the leading edge velocity $v^+$ is in any case between 0.7 and 0.8 of the free-stream velocity. The $x/t$ rays of maximum amplification vary between 0.45 and 0.6, with values increasing with the streamwise location

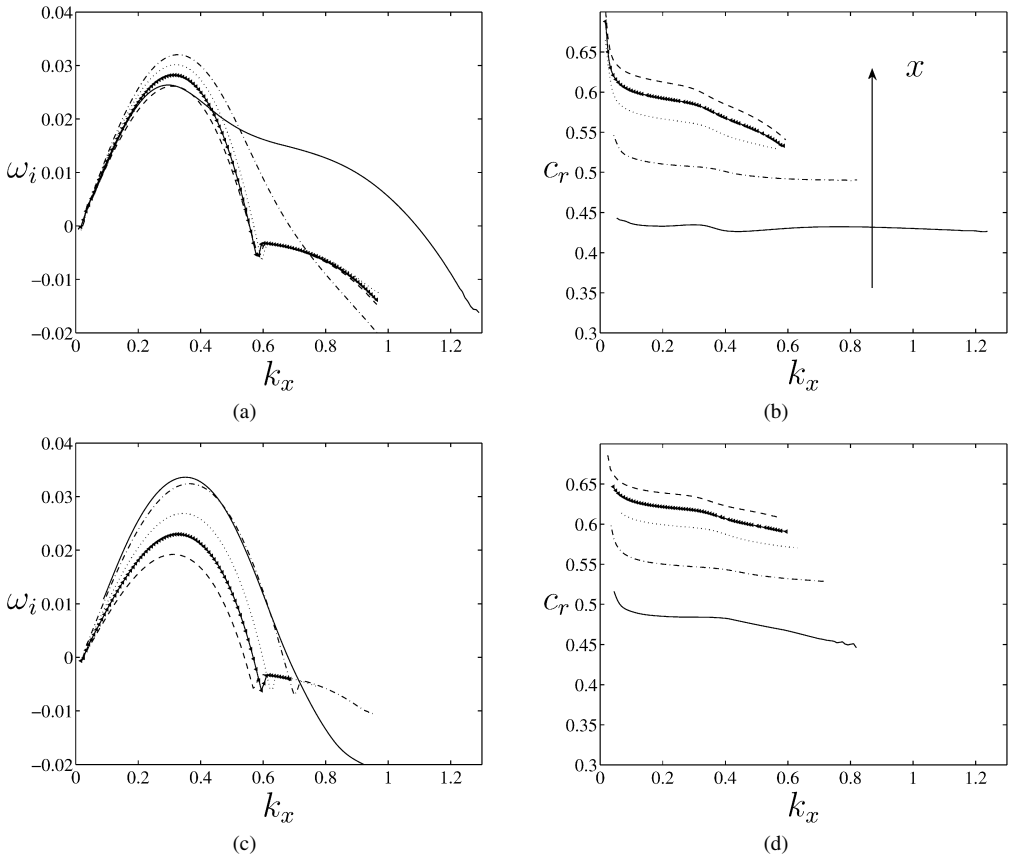


Fig. 5. Temporal growth rates $\omega_i$ and phase speeds $c_r$ versus the streamwise wavenumber $k_x$ for the sinuous instability modes pertaining to the streak induced by the wider screen (a) and (b), and by the narrow screen (c) and (d). The streak profiles are extracted at $x = 71.5$ (solid line), $x = 81$ (dash–dotted line), $x = 95.3$ (dotted line), $x = 104.8$ (line with symbols) and $x = 114.3$ (dash line).

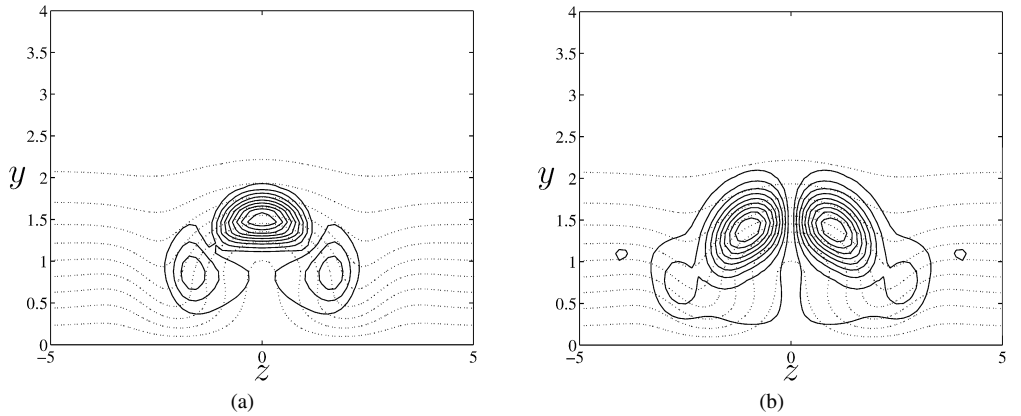


Fig. 6. (a) Cross-stream distribution of the streamwise velocity fluctuations for the varicose temporal mode of streamwise wavenumber $k_x = 0.84$ for the streak extracted at $x = 81$. (b) Streamwise fluctuations for the sinuous mode of streamwise wavenumber $k_x = 0.33$. Contour levels vary from 0.1 to 0.9 of the maximum. The dotted lines display the underlying streak profile.

considered. Also in the case of antisymmetric perturbations the spreading rate of the wave packet decreases for less unstable streak profiles. Relevant differences between the wide and narrow streak are not found for either symmetries. When comparing with the results in [8], it can be noted that for the type of streak considered here, induced by

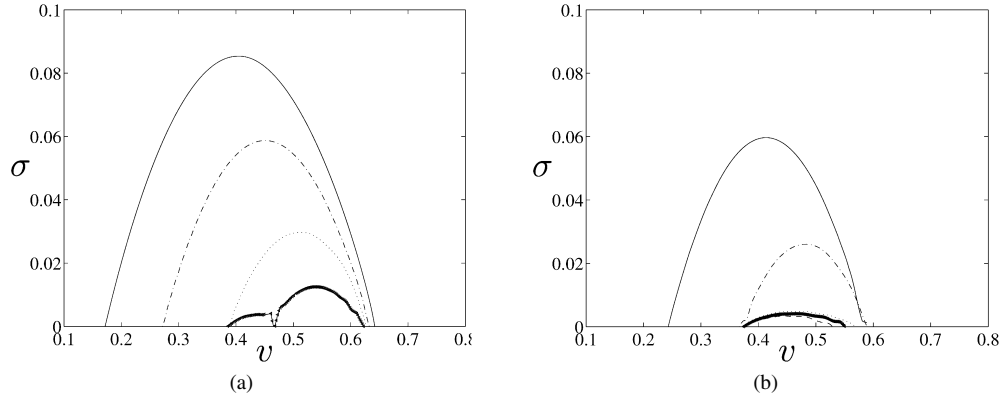


Fig. 7. Temporal growth rates $\sigma$ versus the group velocity $v$ for the varicose instability modes pertaining to the streak induced by the wider screen, (a) and by the narrow screen (b). The streak profiles are extracted at $x = 71.5$ (solid line), $x = 81$ (dash–dotted line), $x = 95.3$ (dotted line), $x = 104.8$ (line with symbols) and $x = 114.3$ (dash line).

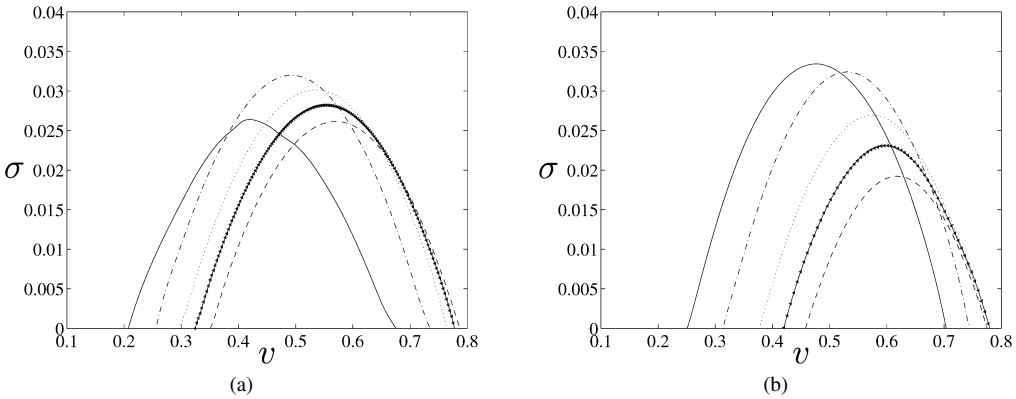


Fig. 8. Temporal growth rates $\sigma$ versus the group velocity $v$ for the sinuous instability modes pertaining to the streak induced by the wider screen, (a) and by the narrow screen (b). The streak profiles are extracted at $x = 71.5$ (solid line), $x = 81$ (dash–dotted line), $x = 95.3$ (dotted line), $x = 104.8$ (line with symbols) and $x = 114.3$ (dash line).

a momentum loss close to the wall, the unstable wave packet is characterised by lower group velocities, almost half of those pertaining to the instability riding on a saturated optimally growing streak.

### *4.3. Instability mechanisms*

In order to examine the instability mechanisms, the distribution of the kinetic energy production terms in the cross-stream $(y, z)$ plane is evaluated. Assuming waves periodic in the streamwise direction, the perturbation kinetic energy equation averaged over the streamwise length of the perturbation reads

$$\frac{\mathrm{d}}{\mathrm{d}t}\left[\int_0^{y_{\max}}\int_0^{\lambda_z}\frac{1}{2}\left(\overline{u^2}+\overline{v^2}+\overline{w^2}\right)\mathrm{d}y\,\mathrm{d}z\right]$$
$$=-\int_0^{y_{\max}}\int_0^{\lambda_z}\frac{\partial U}{\partial y}\overline{uv}\,\mathrm{d}y\,\mathrm{d}z-\int_0^{y_{\max}}\int_0^{\lambda_z}\frac{\partial U}{\partial z}\overline{uw}\,\mathrm{d}y\,\mathrm{d}z-\frac{1}{Re}\int_0^{y_{\max}}\int_0^{\lambda_z}\overline{\boldsymbol{\omega}\cdot\boldsymbol{\omega}}\,\mathrm{d}y\,\mathrm{d}z, \tag{15}$$

where a bar denotes the streamwise average, $\lambda_z$ is the spanwise wavelength of the streak and $\boldsymbol{\omega}$ the perturbation vorticity vector. This balance equation is derived linearising the Navier–Stokes equations around the streak profile $U(y, z)$. The first production term of cross-plane density $-\frac{\partial U}{\partial y}\overline{uv}$ represents the work of the Reynolds stress $\tau_{xy} = -\overline{uv}$

on the wall-normal basic shear $\frac{\partial U}{\partial y}$, while the second production term of density $-\frac{\partial U}{\partial z}\overline{uw}$ is associated with the work of the Reynolds stress $\tau_{xz} = -\overline{uw}$ on the spanwise basic shear $\frac{\partial U}{\partial z}$. The last term represents viscous dissipation.

Considering only temporal modes and further integrating in the wall-normal and spanwise direction, one equation relating the various production terms to the temporal growth rate $\omega_i$ of the wave can be obtained (see also [14]),

$$\omega_i = \frac{\widetilde{T}_y}{2\widetilde{E}} + \frac{\widetilde{T}_z}{2\widetilde{E}} - \frac{\widetilde{D}}{2\widetilde{E}}. \tag{16}$$

In the equation above, the quantity $\widetilde{E}$ is the total perturbation kinetic energy and $\widetilde{D}$ is the viscous dissipation term given by the square of the perturbation vorticity vector. $\widetilde{T}_y$ and $\widetilde{T}_z$ are the perturbation kinetic energy production terms associated with the work of the Reynolds stresses against, respectively, the wall-normal shear $\partial U/\partial y$ and spanwise shear $\partial U/\partial z$ of the basic flow.

The kinetic energy balance is first analysed for the configuration and eigenfunctions displayed in Fig. 6. It is found that the varicose instability is mainly driven by the work of the Reynolds stress $\tilde{\tau}_{uv}$ against the wall-normal shear $\partial U/\partial y$. The cross-stream distribution of the terms appearing in Eq. (15) is displayed in Fig. 9 for the streak profile extracted at $x = 81$, i.e. 50 mm downstream of the wider screen. The shaded areas in the plots represent the region where the density terms exceed 30% of their maxima. As expected, the production terms are largest where the shear of the underlying streak is maximum. The integrated values of the different production/dissipation terms are reported in the caption and in Table 2. Both production terms $\widetilde{T}_y$ and $\widetilde{T}_z$ contribute to the growth rate $\omega_i$, being the first one order of magnitude larger. By comparing with the streamwise velocity fluctuations in Fig. 6(a), it can be noted that the largest perturbation levels are found to correspond with the cross-stream locations of maximum production and also of production associated to the spanwise shear. The viscous dissipation takes place on the top of low-speed region, where the production due to the wall-normal shear is maximum.

Unexpected results are obtained in the case of the sinuous instability: the wall-normal shear is also responsible for this type of instability modes, despite $\tilde{\tau}_{uv}$ and $\partial U/\partial y$ now have opposite spanwise symmetry. For the sinuous mode with $k_x = 0.33$, $\widetilde{T}_y = 0.045$ and $\widetilde{T}_z = 0.002$, that is the production associated with the wall-normal shear $\partial U/\partial y$ is one order of magnitude larger than that associated to its spanwise counterpart $\partial U/\partial z$. The density of perturbation kinetic energy production is displayed in Fig. 10. The distribution of the production term and the fact that the sinuous instability is also mainly induced by the wall-normal shear of the basic flow is able to explain the location of the maximum streamwise velocity fluctuations shown in Fig. 6(b).

It is interesting to compare the results obtained for the streak considered here with those pertaining to the optimal streak computed by Andersson et al. [1]. In particular, for a streak of amplitude $0.36U_\infty$, where the amplitude is defined as half the maximum distortion with respect to the Blasius profile, and for sinuous perturbations with the most amplifying streamwise wavenumber $k_x = 0.6$, the terms in Eq. (16) take the following values. $\omega_i = 0.0338$, $\widetilde{T}_y/2\widetilde{E} = -0.0095$, $\widetilde{T}_z/2\widetilde{E} = 0.0505$, $\widetilde{D}/2\widetilde{E} = 0.0071$. In other words, the spanwise shear is responsible for the antisymmetric sinuous instability and the wall-normal shear weakly counteracts it. Therefore, for the streak considered here, in which the wall-normal shear is dominating over its spanwise counterpart both in term of absolute value and of extension in the cross-stream plane, the shear $\partial U/\partial y$ is responsible also for the amplification of the sinuous antisymmetric waves. Conversely, for the optimal streak computed in [1], characterised by relatively dominating spanwise shear, the sinuous mode is sustained by the work of the Reynolds stress $\tilde{\tau}_{uw}$ against $\partial U/\partial z$. Note that the relative importance of the wall-normal and spanwise shears of the basic flow can be deduced by looking at the slope of the contour levels of the streamwise velocity in a $(y, z)$ plane (cf. Figs. 1 and 6(b) in [1]). The tangent of the angle

Table 2
Values of the terms in the instability balance equation (16) for varicose modes with $k_x = 0.84$ and streaks extracted at different $x$-stations

| | $\widetilde{T}_y$ | $\widetilde{T}_z$ | $\widetilde{D}$ | $\omega_i$ | $\widetilde{T}_y/\widetilde{D}$ | $\widetilde{T}_z/\widetilde{D}$ | Streak |
|---|---|---|---|---|---|---|---|
| $x = 71.5$ | 0.1068 | 0.0023 | 0.0247 | 0.0844 | 4.32 | 0.09 | W |
| $x = 81$ | 0.0809 | 0.0058 | 0.0287 | 0.0581 | 2.82 | 0.20 | W |
| $x = 95.3$ | 0.0468 | 0.0166 | 0.0333 | 0.0301 | 1.40 | 0.50 | W |
| $x = 104.8$ | 0.0266 | 0.0234 | 0.0374 | 0.0126 | 0.71 | 0.62 | W |
| $x = 71.5$ | 0.0777 | 0.0147 | 0.0347 | 0.0576 | 2.24 | 0.42 | N |
| $x = 81$ | 0.0438 | 0.0237 | 0.0410 | 0.0264 | 1.07 | 0.58 | N |

W and N refer to the streak induced by the wide and narrow screen, respectively.

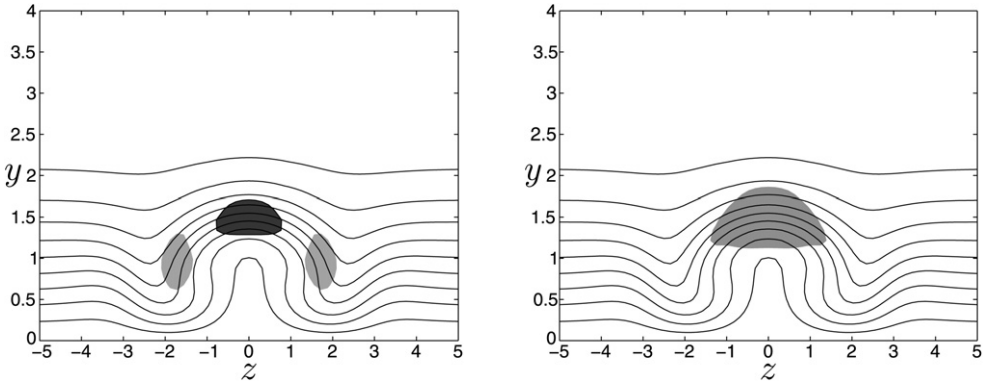


Fig. 9. Density of perturbation kinetic energy production for the streak extracted 50 mm downstream of the wider screen, $x = 81$. The shaded areas represent the region of the cross-stream plane where the terms exceed 30% of their maxima. (a) $\widetilde{T}_y$: dark grey, $\widetilde{T}_z$: light grey. (b) Viscous dissipation. Varicose mode with $k_x = 0.84$. $\omega_i = 0.0581$, $\widetilde{T}_y/2\widetilde{E} = 0.0809$, $\widetilde{T}_z/2\widetilde{E} = 0.0058$, $\widetilde{D}/2\widetilde{E} = 0.0287$.

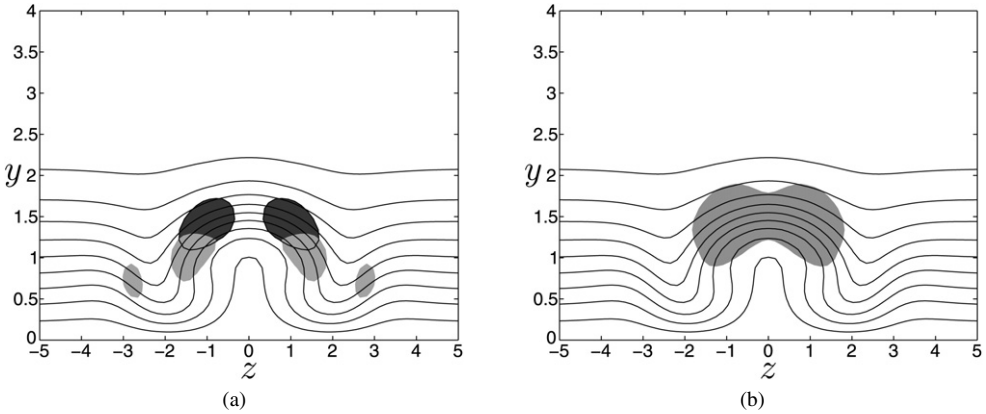


Fig. 10. Same as Fig. 9 for the sinuous mode with $k_x = 0.33$. $\omega_i = 0.0321$, $\widetilde{T}_y/2\widetilde{E} = 0.0453$, $\widetilde{T}_z/2\widetilde{E} = 0.0017$, $\widetilde{D}/2\widetilde{E} = 0.0149$.

$\phi$ between the $z$-axis and the tangent to the streamwise velocity contour level is equal to the ratio between the shears associated to the streak

$$\tan\phi = \frac{\partial U/\partial z}{\partial U/\partial y}.$$

It can be noted in Figs. 9 and 10 that the production zone seems to be wrapped around the boundary of the low-speed streak. Therefore, let us consider the production of the perturbation kinetic energy in a local reference system $(x, n, b)$ where $x$ is the streamwise direction, $n$ the direction parallel to the basic flow velocity gradient, defined by the angle $\phi$ and corresponding to the direction normal to the basic flow vortex lines, and $b$ the third orthogonal axis. The corresponding velocities are denoted $u$, $u_n$ and $u_b$, respectively. In such a reference frame, production is only due to the work of the Reynolds stress $-\overline{uu_n}$ against the local mean shear $\partial U/\partial n$, being the other production term $-\overline{uu_b}\partial U/\partial b = 0$ by definition of the directions $n$ and $b$. Hence, the production for streak instability is due to the velocity fluctuations and Reynolds stress parallel to the local mean flow gradient. Complication is added by the symmetry of the mean flow. It can be seen that owing to such symmetries it is natural to expect that varicose symmetric modes are driven by the wall-normal shear (since symmetric $u$ and $v$ velocities are present in the region of largest shear, $z = 0$), whereas sinuous antisymmetric modes are expected to be induced by the spanwise shear and spanwise velocity fluctuations (antisymmetric fluctuations of $u$ and symmetric $w$ largest on the sides of the streak where the spanwise shear is dominant). However, it is shown by the present results that this is not always the case. In other words, the only mechanism for streak instability is production associated to Reynolds stresses locally parallel to the mean flow gradient and therefore the usual distinction in wall-normal and spanwise directions may not be the most

appropriate. In particular, when considering the sinuous mode depicted in Figs. 6(b) and 10 it can be noted that despite the streamwise $u$ and wall-normal $v$ perturbation velocities are antisymmetric and thus zero in the region of highest wall-normal shear, they still dominate the perturbation production through $-\overline{uv}\partial U/\partial y$ owing to the wide region of strong wall-normal shear.

The energy balance analysis has been repeated for all the streak profiles under considerations, whenever unstable waves are found. The computed values of the integral of the density terms, $\widetilde{T}_y$, $\widetilde{T}_z$ and $\widetilde{D}$ are reported in Table 2 for varicose modes of streamwise wavenumber $k_x = 0.84$ and in Tables 3 and 4 for sinuous modes of streamwise wavenumber $k_x = 0.33$ for the streak induced by the wide and narrow screen, respectively. In the case of varicose modes, the observed decrease of $\omega_i$ when moving downstream can be explained by a significant decrease in the production term $\widetilde{T}_y$. The latter is related to the fast decrease in $\partial U/\partial y$ shown in Fig. 3(a). The perturbation kinetic energy production $\widetilde{T}_z$, associated to the spanwise shear, is slightly increasing with the location $x$ at which the streak instability is considered. As shown in Fig. 3(b), $\partial U/\partial z$ is almost constant in the streamwise direction, however its relative importance in the instability increases. Examining the results pertaining to the narrow streak, it can be noted that $\widetilde{T}_y$ assumes now lower values. This can be explained by the reduced spanwise extension of the horizontal layer of large $\partial U/\partial y$. The ratio between the values of $\widetilde{T}_y$ for the two streaks is roughly of the order of that between the width of the two screens inducing the streaks. The relative importance of the term $\widetilde{T}_z$ is large in the case of the narrow streak, a finding one can explain recalling that the spanwise shear is about 30% larger in the case of the narrow streak.

From the results in Table 3 relative to the sinuous modes, it can be noted that, also in this case, both production terms give a positive contribution to the wave amplification. The work of the Reynolds stress $\tilde{\tau}_{uv}$ against $\partial U/\partial y$ is mainly responsible for the instability. Following the evolution of the wider streak further downstream, where the wall-normal shear has decreased more than its spanwise counterpart, it is found that the term $\widetilde{T}_y$ is still larger than $\widetilde{T}_z$, even though of comparable amplitude. The production associated to the spanwise shear is seen to be the strongest term for a sinuous instability only in the case of the streak induced by the narrow screen (Table 4) and only at the two stations furthest downstream ($x = 104.8$ and $x = 114.3$). The work of the wall-normal shear $\widetilde{T}_y$ is initially of the same order for the two flows under consideration and becomes about twice as much for the wider streak further downstream. Conversely, the work of the Reynolds stress $\tilde{\tau}_{uw}$ against $\partial U/\partial z$ is larger in the case of the narrow streak. However, the larger values of $\widetilde{T}_z$ are not able to more than balance the faster decrease of $\widetilde{T}_y$ observed in the case of the narrow streak and therefore the wide streak is more unstable to sinuous perturbations downstream of $x \approx 81$.

Table 3
Values of the terms in the instability balance equation (16) for sinuous modes on the wider streak with $k_x = 0.33$ and streaks extracted at different $x$-stations

| | $\widetilde{T}_y$ | $\widetilde{T}_z$ | $\widetilde{D}$ | $\omega_i$ | $\widetilde{T}_y/\widetilde{D}$ | $\widetilde{T}_z/\widetilde{D}$ |
|---|---|---|---|---|---|---|
| $x = 71.5$ | 0.0448 | 0.0019 | 0.0212 | 0.0255 | 2.11 | 0.09 |
| $x = 81$ | 0.0453 | 0.0017 | 0.0149 | 0.0321 | 3.04 | 0.11 |
| $x = 95.3$ | 0.0332 | 0.0091 | 0.0122 | 0.0301 | 2.72 | 0.75 |
| $x = 104.8$ | 0.0270 | 0.0125 | 0.0113 | 0.0282 | 2.39 | 1.10 |
| $x = 114.3$ | 0.0220 | 0.0149 | 0.0107 | 0.0261 | 2.05 | 1.39 |

Table 4
Values of the terms in the instability balance equation (16) for sinuous modes on the narrow streak with $k_x = 0.33$ and streaks extracted at different $x$-stations

| | $\widetilde{T}_y$ | $\widetilde{T}_z$ | $\widetilde{D}$ | $\omega_i$ | $\widetilde{T}_y/\widetilde{D}$ | $\widetilde{T}_z/\widetilde{D}$ |
|---|---|---|---|---|---|---|
| $x = 71.5$ | 0.0474 | 0.0021 | 0.0160 | 0.0336 | 2.96 | 0.13 |
| $x = 81$ | 0.0333 | 0.0120 | 0.0132 | 0.0321 | 2.52 | 0.91 |
| $x = 95.3$ | 0.0213 | 0.0177 | 0.0123 | 0.0267 | 1.73 | 1.44 |
| $x = 104.8$ | 0.0157 | 0.0195 | 0.0123 | 0.0229 | 1.27 | 1.58 |
| $x = 114.3$ | 0.0114 | 0.0205 | 0.0126 | 0.0192 | 0.90 | 1.63 |

## 5. Streak breakdown

### 5.1. Varicose breakdown

In order to study the late stages of the transition triggered by the varicose instability, blowing and suction is applied in the numerical simulations. This is localised around $x = 68$ and has a frequency $\omega = 0.36$, see Section 2.2 for further details. An overview of the streak breakdown is displayed in Fig. 11, where dark grey represents the isosurface of positive perturbation streamwise velocity $u' = 0.12$ and light grey depicts the low-speed streak ($u' = -0.12$). The perturbation velocity $u'(x, y, z, t)$ is defined as the difference between the instantaneous streamwise velocity $u(x, y, z, t)$ and its spanwise average $\bar{u}(x, y, t)$. It can be seen in the figure that the amplitude of the symmetric oscillations increases downstream and that this leads to a splitting of the low-speed streak which can be first seen in the lower part of the boundary layer (see light $U$-shaped structures). Comparing the present results with the streamwise velocity contour levels displayed in [2], Figs. 18 and 19, it is evident that the flow structures associated to the streak motion are almost identical to those observed in the experiments. The two regions of positive streamwise velocity on the side of the low-speed region are also oscillating in the spanwise direction in a symmetric pattern.

To identify the vortical structures characteristic of this transition scenario, negative values of the second largest eigenvalue $\lambda_2$ of the Hessian of the pressure (see [23]) are used here. Isosurfaces of negative $\lambda_2$ are displayed in dark in Fig. 12 for the whole transition region. In the figure, the low-speed streak is also shown for comparison. The dominant structures are quasi-streamwise vortices (note that the figure is not at the actual aspect ratio) joining in the middle of the low-speed streak and pointing alternatively upstream and downstream. The latter type becomes prominent at the late stages of the transition process and the breakdown to turbulence is associated to their evolution. These vortices are very similar to those observed in the simulations of transition in a boundary layer subject to free-stream turbulence

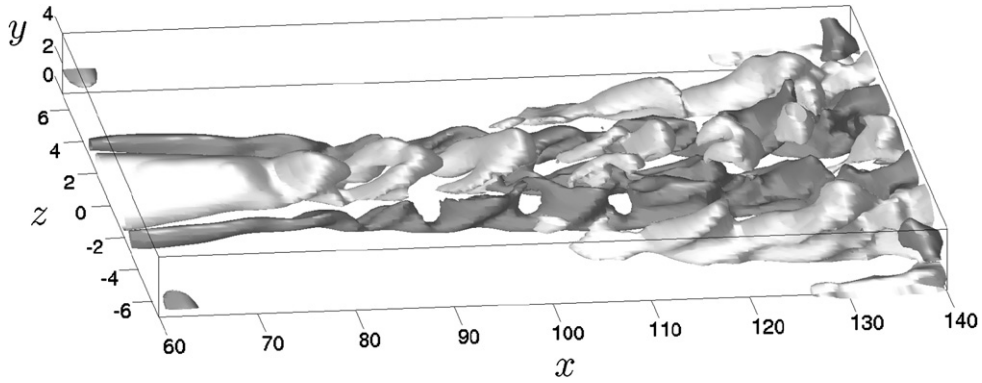


Fig. 11. Instantaneous flow configuration for the varicose breakdown of the streamwise streak. Dark grey represents positive perturbation streamwise velocity ($u' = 0.12$), while light grey indicates the low-speed streak ($u' = -0.12$).

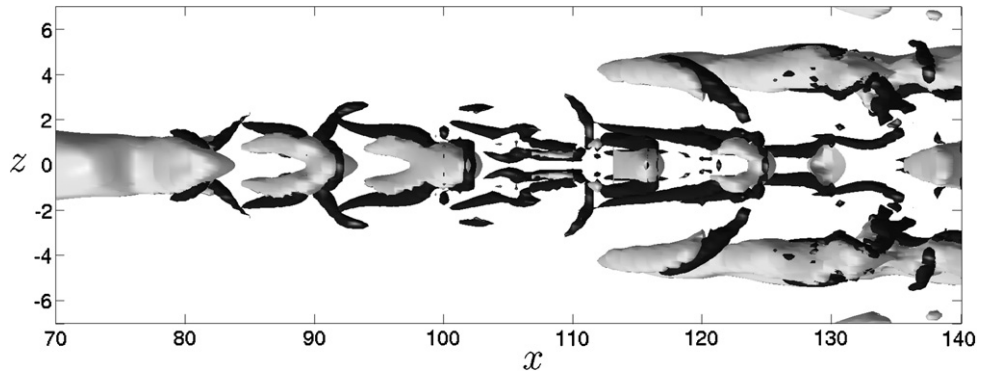


Fig. 12. Top view of an instantaneous flow configuration for the varicose breakdown of the streamwise streak, same as Fig. 11. Light grey represents negative perturbation streamwise velocity ($u' = -0.16$), while dark grey indicates regions of negative $\lambda_2$, used to identify vortical structures.

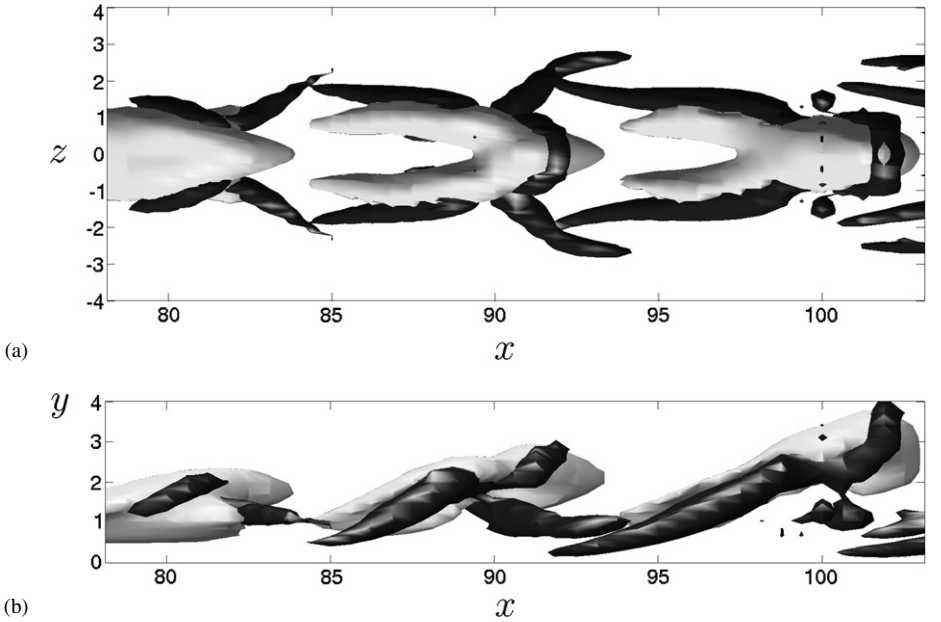


Fig. 13. (a) Top and (b) side view of the flow structures at the varicose breakdown of the streamwise streak. Light grey represents negative perturbation streamwise velocity ($u' = -0.16$), while dark grey indicates regions of negative $\lambda_2$, used to identify vortical structures.

by Brandt et al. [11]. The latter authors identify varicose-like structures in some of the spot precursors considered and refer to them as $V$- and $\Lambda$-structures. More complicated structures can be seen downstream of $x \approx 120$, where transitional flow is present in a larger portion of the computational domain.

A more detailed picture of the relevant vortical structures just before the breakdown is given in Fig. 13, where both a top and a side view of the vortices are reported. It can be seen in the side view in Fig. 13(b) that the $\Lambda$-structures, i.e. the vortices pointing downstream, are tilted away from the wall, whereas the $V$-vortices are found at almost constant $y$-values. They are in fact just slightly inclined towards the wall. It can also be noted that, for $x < 85$, the $V$- and $\Lambda$-structures have comparable amplitude. Further downstream, the $\Lambda$-vortices become longer and occupy almost the whole wavelength of the instability mode, whereas the $V$-structures become wider. At this stage, the splitting of the low-speed streak is more evident. Moving downstream, as the $\Lambda$-vortices grow, their tip deforms into ring-like structures. These are almost aligned in the wall-normal direction and are very similar to the structures observed when transition is induced by the secondary instability of Tollmien–Schlichting waves (see e.g. [7]). In that context, these vortex-rings are also referred to as $\Omega$-vortices.

### 5.2. Sinuous breakdown

Numerical simulations of the streak breakdown triggered by spanwise antisymmetric blowing/suction at the wall (see Section 2.2) are also performed. A picture of the flow in the transition region is shown in Fig. 14, where both positive and negative isosurfaces of the streamwise perturbation velocity $u'$ are displayed in a view from above. The sinuous instability appears as harmonic antisymmetric spanwise oscillation of the low-speed streak. The latter is disrupted at $x \approx 110$. Downstream of this point, positive perturbation velocity is observed in the middle of the computational domain, whereas negative values of $u'$ are attained on the sides. This is due to the fact that the boundary layer profile is fuller, or of more turbulent nature, once the low-speed streak has broken down. Therefore, when compared to the flow on the side of the streak which is still only slightly perturbed, positive perturbation velocity is found.

A detailed study of the breakdown originating from the sinuous streak instability can be found in [10] and it is therefore not repeated here. These authors identified the main structures observed during the transition process. They consist of elongated quasi-streamwise vortices located on the flanks of the low-speed streak. Vortices of alternating

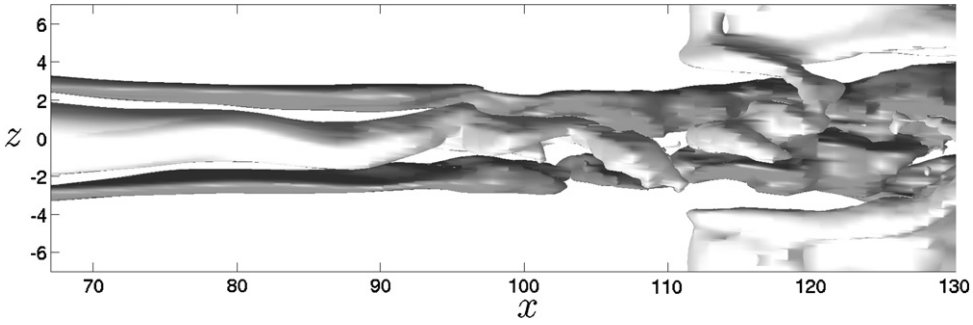


Fig. 14. Top view of an instantaneous flow configuration for the sinuous breakdown of the streamwise streak. Dark grey represents positive perturbation streamwise velocity ($u' = 0.12$), while light grey indicates the low-speed streak ($u' = -0.12$).

sign are overlapping in the streamwise direction in a staggered pattern and they are symmetric counterparts, both inclined away from the wall while following the low-speed region oscillations.

### *5.3. Discussion*

In this section, the late stages of transition initiated by the streak varicose instability are compared with different scenarios previously studied in flat-plate boundary layers. In particular, we consider the transition scenario initiated by the exponential growth of two-dimensional Tollmien–Schlichting waves and their secondary instability (see among others [26,18,36]), transition originating from the streak sinuous instability [10] and the by-pass transition scenario triggered by a pair of oblique waves [4]. In the latter case, streamwise aligned vortices are generated by nonlinear interactions between the oblique waves and, in turn, form streamwise streaks which then become unstable.

The common feature of these scenarios is the presence at the late stages of streamwise streaks and of quasi-streamwise vortices, located on the flanks of the low-speed region and tilted away from the wall. The latter are induced by the amplification of time and spanwise dependent modes (oblique waves). In the classic scenario, the initially growing two-dimensional Tollmien–Schlichting waves are in fact negligible at the breakdown (see also discussion in [4]). In the varicose scenario studied here, oblique waves arise from the streak secondary instability and create the $V$- and $\Lambda$-structures shown in Fig. 13.

In the case of sinuous instability, positive and negative quasi-streamwise vortices are staggered in the streamwise direction, whereas in all other cases the vortices are not staggered but join at the centre of the streak. This difference is due to the spanwise symmetry of the streamwise vorticity of the secondary instabilities. In the case of sinuous streak breakdown, the vorticity distribution is symmetric, whereas $\Lambda$-structures result from an antisymmetric distribution. The common physical process, able to explain the birth of the different structures, is the amplification at the late stages of the streamwise vorticity which can sustain the streak and induce stronger mean shear. In other words, the evolution of streamwise vorticity is characterised by the growth of structures of positive sign on the positive side of the low-speed streak and of negative sign on the negative flank. This is evident in Fig. 12, where it is shown how the $\Lambda$-structures, inducing upward motion inside, soon grow and become dominant, whereas the $V$-vortices disappear at the breakdown.

It is therefore not surprising that the varicose scenario considered here shows strong similarities with transition originating from the secondary instability of Tollmien–Schlichting waves, where the oblique modes of the secondary perturbation are also symmetric. In addition, the similarities with the oblique transition can be explained by the fact that this scenario is characterised by the amplification of streamwise streaks over the oblique waves originally inducing the streamwise vortices. Owing to the symmetric pattern created by the oblique waves with respect to the streaks, the breakdown can be seen as the result of varicose streak instability.

## 6. Summary and conclusions

In the present work, by reproducing numerically the experimental configuration in [2], a single low-speed streak is generated in a laminar boundary layer in order to examine its instability features and the resulting generation of coherent structures.

It is shown that the numerical base flows reproduce the main characteristics of that in [2]. As in the experiments, the most unstable varicose modes have higher frequencies than their sinuous counterpart. However, from the spatio-temporal analysis it is found that the varicose waves travel at lower group velocities. The varicose instability is stronger closer to the generating device but its growth rates decrease faster downstream. Conversely, the sinuous instability is not so affected by the mean shear diffusion and it is more persistent. The sinuous instability is relatively more important for the narrow streak.

The analysis of the kinetic energy production terms reveals that the main contribution to the varicose instability is due to the work of the Reynolds stress $\tau_{xy} = -\overline{uv}$ on the wall-normal basic shear $\partial U/\partial y$, essentially as in Kelvin–Helmholtz instability. However, contrary to intuition, it is found that also the sinuous instability is mainly supported by the wall-normal shear of the basic flow, and not by the term $-\partial U/\partial z\overline{uw}$, associated with the work of the Reynolds stress $\tau_{xz} = -\overline{uw}$ on the spanwise basic shear $\partial U/\partial z$, as previously found for other streaky flows [8]. Therefore, it is not always correct to relate the sinuous instability to the streak spanwise shear and the varicose modes to the streak wall-normal shear. It is shown here that the streak instability is due to the production associated to the Reynolds stress locally parallel to the mean flow gradient and therefore the distinction in wall-normal and spanwise directions may not be the most appropriate. This finding explains why the production zone appears in the cross-stream plane to wrap around the boundary of the low-speed streak for both instability modes.

Direct numerical simulations of the varicose breakdown are performed in order to compare the relevant flow structures with those pertaining to other transition scenarios previously studied. This has allowed to identify universal features of the late stages of transition in boundary layers: streamwise streaks and quasi-streamwise vortices. A physical process common to all the scenarios considered is the amplification at the late stages of those vortices which are able to further sustain the streak and to induce a stronger mean shear. Strong similarities are found between the breakdown initiated by varicose instability and those scenarios displaying the same symmetry of the streamwise vorticity associated to secondary instability modes (see Tollmien–Schlichting induced transition and oblique transition), whereas differences are found with the sinuous breakdown. Note that streaks and streamwise vortices are also found as key elements of the travelling waves around which the turbulent state is suggested to be organised (see [20]).

It was suggested by Schoppa and Hussain [41] that stable streaks may undergo breakdown after the transient amplification of streamwise dependent perturbations, mainly consisting of the spanwise velocity component. The possibility of non-modal growth on streaky base flows has been recently confirmed by Hoepffner et al. [19] for the steady streaks arising from the nonlinear saturation of optimal perturbations. These authors show that, despite such streaks are much more unstable to sinuous modes, both sinuous and varicose perturbations can undergo significant transient amplification. The input/output analysis in [19] might be applied to the base flows computed here, where the two instabilities are in competition, to determine which waves are most amplified after a given time interval, thus considering the initial receptivity phase of the instability. However, this is left to future work.

## References

[1] P. Andersson, L. Brandt, A. Bottaro, D.S. Henningson, On the breakdown of boundary layers streaks, J. Fluid Mech. 428 (2001) 29–60.
[2] M. Asai, M. Minagawa, M. Nishioka, The instability and breakdown of a near-wall low-speed streak, J. Fluid Mech. 455 (2002) 289–314.
[3] K.H. Bech, D.S. Henningson, R.A.W.M. Henkes, Linear and nonlinear development of localized disturbances in zero and adverse pressure gradient boundary layers, Phys. Fluids 10 (1998) 1405–1418.
[4] S. Berlin, M. Wiegel, D.S. Henningson, Numerical and experimental investigations of oblique boundary layer transition, J. Fluid Mech. 393 (1999) 23–57.
[5] A. Bers, Space–time evolution of plasma instabilities – absolute and convective, in: M.N. Rosenbluth, R.Z. Sagdeev (Eds.), Handbook of Plasma Physics, vol. 1, North-Holland, Amsterdam, 1983, pp. 451–517.
[6] F.P. Bertolotti, T. Herbert, P.R. Spalart, Linear and nonlinear stability of the Blasius boundary layer, J. Fluid Mech. 242 (1992) 441–474.
[7] V. Borodulin, V. Gaponenko, Y. Kachanov, D. Meyer, U. Rist, Q. Lian, C. Lee, Late-stage transitional boundary-layer structures. Direct numerical simulation and experiment, Theoret. Comput. Fluid Dynamics 15 (5) (2002) 317–337.
[8] L. Brandt, C. Cossu, J.-M. Chomaz, P. Huerre, D.S. Henningson, On the convectively unstable nature of optimal streaks in boundary layers, J. Fluid Mech. 485 (2003) 221–242.
[9] L. Brandt, C. Cossu, D.S. Henningson, J.-M. Chomaz, P. Huerre, Numerical studies of streak instability in boundary layers, in: Proceeding IUTAM Symposium Laminar-Turbulent Transition, Bangalore, 2006, pp. 121–126.
[10] L. Brandt, D.S. Henningson, Transition of streamwise streaks in zero-pressure-gradient boundary layers, J. Fluid Mech. 472 (2002) 229–262.
[11] L. Brandt, P. Schlatter, D.S. Henningson, Transition in boundary layers subject to free-stream turbulence, J. Fluid Mech. 517 (2004) 167–198.
[12] K.S. Breuer, J.H. Haritonidis, The evolution of a localized disturbance in a laminar boundary layer. Part 1. Weak disturbances, J. Fluid Mech. 220 (1990) 569–594.

[13] K.T. Christensen, R.J. Adrian, Statistical evidence of hairpin vortex packets in wall turbulence, J. Fluid Mech. 431 (2001) 433–443.
[14] C. Cossu, L. Brandt, On Tollmien–Schlichting-like waves in streaky boundary layers, Eur. J. Mech./B Fluids 23 (2004) 815–833.
[15] I. Delbende, J.-M. Chomaz, Nonlinear convective/absolute instabilities of parallel two-dimensional wakes, Phys. Fluids 10 (1998) 2724–2736.
[16] I. Delbende, J.-M. Chomaz, P. Huerre, Absolute and convective instabilities in the Batchelor vortex: a numerical study of the linear impulse response, J. Fluid Mech. 355 (1998) 229–254.
[17] D.S. Henningson, A. Lundbladh, A.V. Johansson, A mechanism for bypass transition from localized disturbances in wall-bounded shear flows, J. Fluid Mech. 250 (1993) 169–207.
[18] T. Herbert, Secondary instability of boundary-layers, Annu. Rev. Fluid Mech. 20 (1988) 487–526.
[19] J. Hoepffner, L. Brandt, D.S. Henningson, Transient growth on boundary layer streaks, J. Fluid Mech. 537 (2005) 91–100.
[20] B. Hof, C.W.H. van Doorne, J. Westerweel, F.T.M. Nieuwstadt, H. Faisst, B. Eckhardt, H. Wedin, R. Kerswell, F. Waleffe, An experimental observation of travelling waves in pipe flow, Science 305 (5690) (2004) 1594–1598.
[21] P. Huerre, Open shear flow instabilities, in: G.K. Batchelor, H.K. Moffatt, M.G. Worster (Eds.), Perspectives in Fluid Dynamics, Cambridge University Press, Cambridge, 2000, pp. 159–229.
[22] P. Huerre, M. Rossi, Hydrodynamic instabilities in open flows, in: C. Godrèche, P. Manneville (Eds.), Hydrodynamic and Nonlinear Instabilities, Cambridge University Press, Cambridge, 1998, pp. 81–294.
[23] J. Jeong, F. Hussain, W. Schoppa, J. Kim, Coherent structures near the wall in a turbulent channel flow, J. Fluid Mech. 332 (1997) 185–214.
[24] J. Jiménez, A. Pinelli, The autonomous cycle of near wall turbulence, J. Fluid Mech. 389 (1999) 335–359.
[25] J. Jiménez, M.P. Simens, Low dimensional dynamics of a turbulent wall flow, J. Fluid Mech. 435 (2001) 81–91.
[26] Y.S. Kachanov, Physical mechanism of laminar boundary-layer transition, Annu. Rev. Fluid Mech. 26 (1994) 411–482.
[27] G. Kawahara, J. Jiménez, M. Uhlmann, A. Pinelli, The instability of streaks in near-wall turbulence, Tech. Rep., NASA – Stanford University Center for Turbulence Research, Annual Research Briefs, 1998, pp. 155–170.
[28] H.T. Kim, S.J. Kline, W.C. Reynolds, The production of turbulence near a smooth wall in a turbulent boundary layer, J. Fluid Mech. 50 (1971) 133–160.
[29] S.J. Kline, W.C. Reynolds, F.A. Schraub, P.W. Runstadler, The structure of turbulent boundary layers, J. Fluid Mech. 30 (1967) 741–773.
[30] M.T. Landahl, A note on an algebraic instability of inviscid parallel shear flows, J. Fluid Mech. 98 (1980) 243–251.
[31] A. Lundbladh, S. Berlin, M. Skote, C. Hildings, J. Choi, J. Kim, D.S. Henningson, An efficient spectral method for simulation of incompressible flow over a flat plate, Technical Report KTH/MEK/TR-99/11-SE, KTH, Department of Mechanics, Stockholm, 1999.
[32] M.R. Malik, T.A. Zang, M.Y. Hussaini, A spectral collocation method for the Navier–Stokes equations, J. Comp. Phys. 61 (1985) 64–88.
[33] M. Matsubara, P.H. Alfredsson, Disturbance growth in boundary layers subjected to free stream turbulence, J. Fluid Mech. 430 (2001) 149–168.
[34] M. Nishioka, M. Asai, S. Iida, Wall phenomena in the final stage of transition to turbulence, in: R. Eppler, H.F. Fasel (Eds.), Laminar-Turbulent Transition, Springer, Berlin, 1981, pp. 113–126.
[35] J. Nordström, N. Nordin, D.S. Henningson, The fringe region technique and the Fourier method used in the direct numerical simulation of spatially evolving viscous flows, SIAM J. Sci. Comp. 20 (1999) 1365–1393.
[36] U. Rist, H. Fasel, Direct numerical simulation of controlled transition in a flat-plate boundary layer, J. Fluid Mech. 298 (1995) 211–248.
[37] S.K. Robinson, The kinematics of turbulent boundary layer structure, Tech. Rep. TM 103859, NASA, 1991.
[38] N.D. Sandham, L. Kleiser, The late stages of transition to turbulence in channel flow, J. Fluid Mech. 245 (1992) 319–348.
[39] P.J. Schmid, D.S. Henningson, Stability and Transition in Shear Flows, Springer, New York, 2001.
[40] W. Schoppa, F. Hussain, Genesis and dynamics of coherent structures in near-wall turbulence: a new look, in: R.L. Panton (Ed.), Self-Sustaining Mechanisms of Wall Turbulence, Computational Mechanics Publications, Southampton, 1997, pp. 385–422 (Chapter 7).
[41] W. Schoppa, F. Hussain, Coherent structure generation in near-wall turbulence, J. Fluid Mech. 453 (2002) 57–108.
[42] M. Skote, J.H. Haritonidis, D.S. Henningson, Varicose instabilities in turbulent boundary layers, Phys. Fluids 14 (2002) 2309–2323.
[43] J.D. Swearingen, R.F. Blackwelder, The growth and breakdown of streamwise vortices in the presence of a wall, J. Fluid Mech. 182 (1987) 255–290.
[44] F. Waleffe, On a self-sustaining process in shear flows, Phys. Fluids 9 (1997) 883–900.